The multi-scale structure of the atmospheric energetic constraints on global-averaged precipitation

Miguel Nogueira*
Instituto Dom Luiz, Faculdade de Ciências da Universidade de Lisboa
* corresponding author email: mdnogueira@fc.ul.pt

Abstract

This study presents a multi-scale analysis of cross-correlations based on Haar fluctuations of global-averaged anomalies of precipitation (P), precipitable water vapor (PWV), surface temperature (T) and atmospheric radiative fluxes. The results revealed an emergent transition between weak correlations at sub-yearly time-scales (down to ~5-days) to strong correlations at time-scales larger than about ~1-2 years (up to ~1-decade). At multi-year time-scales, (i) Clausius-Clapeyron becomes the dominant control of PWV ($\rho_{PWV,T}\approx0.9$); (ii) surface temperature averaged over global-land and over global-ocean (SST) become strongly correlated ($\rho_{Tland,SST}\sim0.6$); (iii) global-averaged precipitation variability is dominated by energetic constraints - specifically the surface downwelling longwave radiative flux (DLR) ($\rho_{P,DLR}\approx-0.8$) displayed stronger correlations than the direct response to T fluctuations; (iv) cloud effects are negligible for the energetic constraints in (iii), which are dominated by clear-sky DLR. At sub-yearly time-scales, all correlations underlying these four results decrease abruptly towards negligible values. Such a transition has important implications to understand and quantify the climate sensitivity of the global hydrological cycle. The validity of the derived correlation structure is demonstrated by reconstructing global precipitation time-series at 2-year resolution, relying on the emergent strong correlations (P vs clear-sky DLR). Such a simple linear sensitivity model was able to reproduce observed P anomaly time-series with similar accuracy to an (uncoupled) atmospheric model (ERA-20CM), and two climate reanalysis (ERA-20C and 20CR). The linear sensitivity breaks down at sub-yearly time-scales, where the underlying correlations become negligible. Finally, the relevance of the multi-scale framework and its potential for stochastic downscaling applications is demonstrated by deriving accurate monthly P probability density functions (PDFs) from

the reconstructed 2-year P time-series based on scale-invariant arguments alone. The derived monthly PDFs outperforming the statistics simulated by ERA-20C, 20CR and ERA-20CM in reproducing observations.

1. Introduction

The precipitation response to changes in increased concentrations of greenhouse gases is a central topic for the climate science community. Although its regional variability is essential to determine the societal impacts, global-averaged precipitation is an important first-order climate indicator, and a measure of the global water cycle, that must be accurately simulated if robust climate projections are to be obtained across a wide range of spatial and temporal scales.

However, even the long-term response of global-averaged precipitation is still poorly understood, constrained and simulated (Collins et al., 2013; Allan et al., 2014; Hegerl et al., 2015), largely due to the limited knowledge on the complex interactions between the key components of the atmospheric branch of the water cycle and its forcing mechanisms. This problem is tackled here by employing a multi-scale analysis framework to study the global-averaged precipitation variability, and its relation to two key governing mechanisms: the Clausius-Clapeyron relationship and the constraints imposed by the atmospheric energy balance.

The Clausius-Clapeyron relationship is a well-known mechanism controlling the variability of the global water cycle. Assuming constant relative humidity, it implies that fractional changes in global-averaged precipitable water vapor $(\Delta PWV/PWV)$ are linearly related to fluctuations of global-averaged near-surface air temperature (ΔT) (e.g. Held & Soden, 2006; Schneider et al., 2010):

$$\frac{\Delta PWV}{PWV} \approx \alpha_{PWV,T}\Delta T, \qquad (1)$$

where $\alpha_{PWV,T} \approx 0.07$ K^{-1} at temperatures typical of the lower troposphere. Numerous studies have provided a robust confirmation for the Clausius-Clapeyron mechanism at multi-decadal to centennial time-scales, while also reporting an analogous linear response of global-averaged precipitation to surface temperature fluctuations (see e.g. Schneider et al., 2010; Trenberth, 2011; O'Gorman et al., 2012; and Allan et al., 2014 for reviews). In general, these previous investigations agree on the ~7%/K sensitivity coefficient for precipitable water vapor. However, there is large spread on the global precipitation sensitivity coefficient estimates, typically in the 1%/K to 3%/K range.

A widely recognized explanation for the sub-Clausius-Clapeyron sensitivity of precipitation to temperature fluctuations at long temporal scales comes from the atmospheric energy balance (Allen & Ingram, 2002; Stephens & Ellis, 2008; Stephens & Hu, 2010). Specifically, averaging over the global atmosphere, the latent heat flux associated with precipitation formation (L_VP, with P being the global-averaged precipitation flux and L_V the latent heat of vaporization) should be in balance with the net atmospheric radiative flux (R_{atm}) and the surface sensible flux (F_{SH}):

$$L_V P + R_{atm} + F_{SH} \approx 0, \qquad (2)$$

Equation (2) represents a general state of radiative convective equilibrium (Pauluis & Held, 2002), with energy fluxes defined positive for atmospheric gain, and negative otherwise.

If the Clausius-Clapeyron relationship was the dominant mechanism controlling the response of atmospheric moisture content and the global water cycle to temperature fluctuations, then global-averaged precipitable water vapor and precipitation could be expected to be strongly correlated to surface temperature. Previously Gu and Adler (2011, 2012) found strong correlations between the inter-annual variability of global-averaged precipitable water vapor and surface temperature, in tight agreement with the Clausius-Clapeyron mechanism. However, they found weaker (yet significant) correlations between the inter-annual variability of global-averaged precipitation and surface temperature, raising doubts on whether the Clausius-Clapeyron mechanism could be directly extendable to global precipitation. Notice, however, that these results focusing on a single temporal scale might not represent the entire picture

A further source of complexity comes from the fact that precipitation and other relevant atmospheric variables (including temperature, atmospheric moisture, wind, etc.) display a complex statistical structure, with significant variability over a wide range of temporal scales, and with the possibility of different mechanisms governing variability at different time-scales (see e.g. Lovejoy & Schertzer, 2013 for a comprehensive review). Furthermore, it has been shown that this complex multiscale structure plays a role (at least) as important and the large amplitude periodic components, namely diurnal and seasonal cycles (Lovejoy, 2015; Nogueira, 2017a). However, our understanding of the underlying governing mechanisms at different time-scales remains largely elusive, representing a central problem for future improvements to climate simulation and projection.

Recently, Nogueira (2018) analyzed satellite-based observational datasets, a long Global Climate Model (GCM) simulation and reanalysis products and found a tight correlation (~0.8) between anomaly (deseasonalized) time-series of global-averaged precipitable water vapor and surface temperature, which emerged at time-scales larger than ~1-2 years. In contrast, at smaller time-scales the correlation decreased rapidly towards negligible values (<0.3). In other words, the Clausius-Clapeyron relationship is the dominant mechanism of atmospheric moisture anomalies at multi-year time-scales, but not at sub-yearly time-scales. Nogueira (2018) also found that the magnitude of the correlations between anomaly time-series for global-averaged precipitation and surface temperature was negligible at sub-yearly time-scales, while at multi-year time-scales the results showed large spread amongst different data-sets, ranging between negligible (<0.3) and strong (~0.8) correlation values. Building on this previous study, here the multi-scale analysis of the mechanisms governing global precipitation variability was extended, including the energetic constraints on precipitation represented in Eq. (2). The manuscript is organized as follows: section 2 describes the considered datasets and the multi-scale analysis framework; the results of multi-scale correlation analysis on precipitation variability are presented and discussed in section 3; in section 4 the validity of the linear sensitivity correlations derived from the multi-scales analysis is demonstrated by employing a simple linear model to reconstruct global-averaged precipitation time-series from energetic constraints. At sub-yearly time-scales, where the correlations break down, it is shown in section 5 how the monthly statistics can be reproduced by employing a stochastic downscaling algorithm based on scale-invariant symmetries of precipitation. Finally, the main conclusions are summarized and discussed in section 6.

2. Data and Methodology

2.1. Data sets

Precipitation observations were obtained from the Global Precipitation Climatology Project (GPCP) version 2.3 monthly precipitation dataset (Adler et al., 2003), which covers the full globe at 2.5º resolution from 1979 to present. Gridded datasets of monthly average surface temperatures were obtained from the Goddard Institute for Space Studies (GISSTEMP) analysis (Hansen et al., 2010), which covers the globe at 2º resolution from 1880 to present, with the values provided as anomalies relative to the 1951-1980 reference period. GISSTEMP blends near-surface air temperature measurements from meteorological stations (including Antarctic stations) with a reconstructed sea surface temperature (SST) dataset over oceans. Observations of atmospheric radiative fluxes were obtained from the National Aeronautics and Space Administration (NASA) Clouds and the Earth's Radiant Energy System, Energy Balanced and Filled (CERES-EBAF) Edition 4.0 (Loeb et al., 2009), a monthly dataset covering the full globe at 1º resolution from March/2000 to June/2017.

Two state-of-the-art reanalyses of the twentieth-century were considered in the present study. One was the National Oceanic and Atmospheric Administration Cooperative institute for Research in Environmental Sciences (NOAA-CIRES) twentieth-century reanalysis (20CR) version 2c (Compo et al., 2011), which covers the full globe at 2º resolution, spanning from 1851 to 2014. Only surface pressure observations and reports are assimilated in this reanalysis. SST boundary conditions are obtained from 18 members of pentad Simple Ocean Data Assimilation with Sparse Input (SODAsi) version 2, with the high latitudes corrected to the Centennial in Situ Observation-Based Estimates of the Variability of SST and Marine Meteorological Variables, version 2 (COBE-SST2). Here, global-mean time-series of precipitation, precipitable water vapor, near-surface temperature, SST, and atmospheric radiative fluxes were obtained from 20CR at daily resolution for the 1900-2010 period. Notice that the net atmospheric radiative flux cannot be obtained from 20CR, because the incoming solar radiation at the top of the atmosphere is not available for this dataset, due to an error with output processing.

The other reanalysis considered in the present study was the European Centre for Medium-Range Weather Forecasts (ECMWF) twentieth-century reanalysis (ERA-20C, Poli et al., 2015), which covers the full globe at 1º resolution spanning from 1900-2010. It assimilates marine surface winds from the International Comprehensive Ocean-Atmosphere Data Set version 2.5.1 (ICOADSv2.5.1) and surface and mean-sea-level pressure from the International Surface Pressure Databank version 3.2.6 (ISPDv3.2.6) and from ICOADSv2.5.1. SST boundary conditions are obtained from the Hadley Centre Sea Ice and Sea Surface Temperature data set version 2.1 (HadISST2.1). Global-mean time-series of precipitation, precipitable water vapor, near-surface temperature, SST, and atmospheric radiative fluxes were obtained from ERA-20C at daily resolution for the 1900-2010 period.

Finally, the uncoupled ECMWF twentieth-century ensemble of ten atmospheric model integrations (ERA-20CM, Hersbach et al., 2015) was considered, which uses the same model, grid, initial conditions, radiative and aerosol forcings as ERA-20C. However, no observations are assimilated, the simulation is integrated continuously over the full 1900-2010 period, and SST is prescribed by an ensemble of realizations from HadISST2.1, including one control simulation and nine simulations with perturbed SST and sea-ice concentration. A 10-member ensemble of global-mean time-series of precipitation, precipitable water vapor, near-surface temperature, SST, and atmospheric radiative fluxes were obtained from ERA-20CM at monthly resolution for the 1900-2010 period. Considering ERA-20CM allowed to test the sensitivity of the multi-scale correlation structure derived from ERA-20C to data assimilation, but different atmospheric evolutions associated with perturbations to the forcing fields (particularly to SST).

Notice that the clear-sky radiative fluxes considered here obtained from ECMWF datasets are computed for the same atmospheric conditions of temperature, humidity, ozone, trace gases and aerosol, but assuming that the clouds are not there. Clear-sky estimates from ERA-20C and ERA-20CM cover the full globe area and not just the cloud free regions at each time instant. However, they are available for net radiative fluxes, but not for downwelling or upwelling radiation fluxes.

2.2. Multi-scale correlation analysis

Consider two time-series, y, and y', with N data points each. Here the goal is to study the correlation between the fluctuations $\Delta y(\Delta t)$ and $\Delta y'(\Delta t)$ at different time-scales Δt. Due to the strong yearly cycle present in the considered time-series, the periodic seasonal trend was first eliminated by subtracting the long-term average (over all the years in the record) of each calendar day (or month, depending on temporal resolution):

$$y_{ds}(i) = y(i) - \langle y \rangle_d, \qquad (3)$$

where y_{ds} is the deseasonalized anomalies time-series.

Traditionally, fluctuations are defined by the difference $\Delta y(\Delta t) = y(t + \Delta t) - y(t)$. However, it has been shown that such definition is only appropriate for fluctuations increasing with time-scale (Lovejoy and Schertzer, 2013). Consequently, the traditional definition is not useful for the present study, since the fluctuations for most atmospheric variables time-series (including temperature, rain, wind, water vapor, amongst others) decrease with increasing time-scale over the tens of days to tens of years range (e.g. Lovejoy and Schertzer, 2013; Lovejoy, 2015; Lovejoy et al., 2017; Nogueira, 2017a; 2017b; 2018). In this sense, here the fluctuations were defined using the Haar wavelet, which is appropriate for the full range of time-scales and all atmospheric variables considered, in both cases where fluctuations increase or decrease with time-scale. Furthermore, correlations computed from Haar fluctuation time-series also avoid the low frequency biases that emerge in standard correlation analysis due to climate variability (see Lovejoy et al. (2017) for a detailed description of the Haar fluctuations and correlations of Haar fluctuations).

The Haar fluctuations are simply defined as the difference of the means from $t + \Delta t/2$ to $t + \Delta t/2$ and from t to $t + \Delta t/2$, i.e.:

$$(\Delta y(\Delta t))_{Haar} = \frac{2}{\Delta t}\int_{t+\Delta t/2}^{t+\Delta t} y(t)dt - \frac{2}{\Delta t}\int_{t}^{t+\Delta t/2} y(t)dt, \quad (4)$$

For the sake of simplicity, henceforth the fluctuation notation $\Delta y(\Delta t)$ will be employed to refer to Haar fluctuations (i.e. $\Delta y(\Delta t) \equiv (\Delta y(\Delta t))_{Haar}$). A Haar fluctuation time-series was computed by employing Equation 4 at each instant of the deseasonalized anomalies time-series for each variable considered. Finally, at each time-scale, Δt, the correlation coefficient, ρ, of the corresponding Haar fluctuations time-series was computed for each pair of variables considered.

Notice that, in computing correlations at time-scales larger than two times the original time-series resolution, there is overlapping of the data-points considered in computing the Haar fluctuations. While this could introduce spurious effects in the computed correlations, previous works have shown the robustness of the Haar fluctuation-based correlations methodology used here (e.g. Lovejoy et al., 2017). Additionally, the analogous method of Detrended Cross-Correlation Analysis has also been employed on overlapping windows and demonstrated to provide accurate correlation estimates at different time-scales using overlapping windows(see e.g. Podobnik & Stanley, 2008; Podobnik et al., 2011; Piao and Fu, 2016). In fact, in Section 3 below it is shown that identical correlation structures are obtained between correlations of Haar fluctuations and Detrended Cross-Correlation Analysis. Since the multi-scale cross-correlation structure obtained with Haar fluctuations is identical to the results using Detrended Cross-Correlations Analysis, it is assumed that critical points for the 95% significance level of Haar fluctuation correlations are identical to the ones demonstrated by Podobnik et al. (2011) for Detrended Cross-Correlation Analysis using overlapping windows, where the significant values can vary between values below 0.1 and up to about 0.4, depending on the time series length, the considered time-scale, and the power law exponents of both time-series. In this sense, here it is assumed that correlation magnitudes below 0.3 are nonsignificant, and that magnitudes in the 0.3 to 0.4 range should be interpreted with care.

3. Analysis of the mechanisms governing P variability across time-scales

3.1. Multi-scale structure of the atmospheric water cycle response to surface temperature fluctuations

The correlations between Haar fluctuations time-series revealed strong correlations (~0.9) between deseasonalized anomaly time-series for global-averaged precipitable water vapor and near surface temperature (or, alternatively, SST) at multi-year time-scales (Fig. 1a). However, as the time-scale decreases there is a transition in the correlation structure, and negligible correlations (<0.3) emerge at sub-yearly time-scales. This result suggested that the Clausius-Clapeyron relationship (see Eq. (1)) holds to a very good approximation at multi-year time-scales, but not at sub-yearly time-scales. Interestingly, Lovejoy et al. (2017) computed the Haar fluctuation correlations for GISSTEMP surface temperatures and found a similar transition in the multi-scale correlation structure of SST against global-averaged surface temperature, with low-correlations at time-scales below a few months and strong correlations (~0.8) at multi-year time-scales. Notice that the latter strong correlations weren't surprising, since SST was a major component in their definition of global-averaged surface temperature (which for GISSTEMP uses SST over the ocean pixels and 2-meter air temperature over land pixels). Nonetheless, Lovejoy et al. (2017) also found a similar transition for the correlation between SST and near-surface air temperature averaged over global-land, with maximum correlation values ~0.6 at multi-year time-scales. The transition in the correlation structure between SST and global-land temperature was confirmed here for ERA-20C, ERA-20CM, 20CR and GISSTEMP (Fig. 1b). Thus, the present results support Lovejoy et al. (2017) argument that these abrupt correlation changes correspond to a fundamental behavioral transition, where the atmosphere and the oceans start to act as a single coupled system. Furthermore, the results presented here suggest that precipitable water vapor anomalies at multi-year resolution can be derived, to a very good approximation, from SST alone.

Nogueira (2018) also reported a transition in the multi-scale correlation structure between deseasonalized anomaly time-series of global-averaged precipitation and surface temperature (considering SST over the oceans and 2-m air temperature over land), with negligible values at sub-yearly time-scales, but with large spread in the magnitude of the multi-year correlations, ranging between ~0.3 and ~0.8. Here, a similar result was found for the multi-scale correlations structure between global-averaged precipitation and surface temperature and, also, global-averaged precipitation and SST (Fig. 1c), with large spread in correlation magnitude at multi-year time-scales (~0.7 in ERA-20C and ERA-20CM, ~0.6 in 20CR, and <0.4 in observations). Furthermore, considering different timelags in computing the cross-correlations between precipitation and surface temperature did not reveal the presence of significant lagged correlations over the daily to decadal time-scale range.

3.2. Multi-scales structure of the energetic constraints to precipitation variability

A study of the circulation component of the precipitation response to temperature fluctuations requires a detailed representation of several spatially heterogeneous variables and their nonlinear interactions. An alternative path towards understanding global-averaged precipitation temporal variability was taken in the present investigation, focusing on the constraints imposed by the atmospheric energy balance represented in Equation (2). Fig. 2a (solid lines) shows that the estimated multi-scale correlation coefficients between the deseasonalized anomaly time-series for precipitation and net atmospheric radiative fluxes were strongly (negatively) correlated at multi-year time-scales ($\rho \sim -0.8$ in ERA-20C, ERA-20CM and observations), in agreement with the balance in Equation (2). In contrast, at sub-yearly time-scales the correlation magnitude decreased rapidly, changed sign around monthly time-scales, and reached values ~0.4 at time-scales below about 10 days.

Considering the combined effect of the net atmospheric radiative fluxes and sensible heat flux in Equation (2) slightly increased the (positive) correlations at sub-monthly time-scales (Fig. 2a, dashed lines), although the absolute changes are essentially below 0.1. More importantly, Fig. 2a shows that the magnitude of the correlation at multi-year time-scales between global-averaged precipitation and net atmospheric radiative fluxes is significantly larger than when the combined effect of net atmospheric radiative fluxes and sensible heat flux were considered. Indeed, the correlation between global-averaged precipitation and sensible heat flux displayed values up to about 0.5 at sub-monthly time-scales, but essentially <0.4 at multi-year time-scales (Fig. 2a, dot-dashed lines). Given the results in Fig. 2a, the following linear relation was hypothesized: $L_V \Delta P \approx c_1 \times (-\Delta R_{atm}) + c_2$, where c_1 and c_2 are arbitrary constants, and Δ represents fluctuations taken as deseasonalized anomalies at multi-year resolutions. At sub-yearly time-scales this simplification is not adequate, since the correlations between global-averaged precipitation and net atmospheric radiative fluxes becomes negligible. In other words, the energy balance represented in Equation (2) doesn't represent the dominant constraint on precipitation variability at sub-yearly time-scales, most likely due to non-negligible changes in atmospheric heat storage.

The analysis was extended by decomposing net atmospheric radiative fluxes into its net atmospheric longwave and shortwave radiative flux components, i.e. $R_{atm} = R_{LW,net} + R_{SW,net}$. On the one hand, the correlation between global-averaged precipitation and net atmospheric radiative fluxes is nearly identical to the correlation between global-averaged precipitation and net atmospheric longwave radiative fluxes (i.e. $\rho_{P,R_{atm}} \approx \rho_{P,R_{LW,net}}$) over the full range of time-scales considered (Fig. 2b). On the other hand, $\rho_{P,R_{SW,net}}$ also displayed significant values (~0.6) at multi-year time-scales, but the latter magnitude was nearly 0.2 lower when compared to $\rho_{P,R_{atm}}$ and $\rho_{P,R_{LW,net}}$ (Fig. 2b). Consequently, the above linear relationship for multi-scale P anomalies was further refined as $L_V \Delta P \approx c_1 \times (-\Delta R_{atm}) + c_2 \approx c_3 \times (-\Delta R_{LW,net}) + c_4$, where c_3 and c_4 are arbitrary constants. Subsequently, the net atmospheric longwave radiative flux was further decomposed into the top-of-atmosphere (TOA) and surface net longwave fluxes, i.e. $R_{LW,net} = R_{LW,TOA} + R_{LW,SFC}$. At multi-year time-scales, $\rho_{P,R_{atm}} \approx \rho_{P,R_{LW,SFC}}$ (Fig. 2c), suggesting that the surface net longwave radiative fluxes provide the main constraint to global-averaged precipitation variability. The correlation between global-averaged precipitation and TOA longwave radiative fluxes also displayed significant values at multi-year time-scales, up to ~-0.6 in ERA-20C and ERA-20CM datasets, but much lower in 20CR where the magnitude of the correlation was < 0.4 at multi-year time-scales. Nonetheless, the former correlations (in ERA-20C and ERA-20CM) were in better agreement with observations, suggesting that significant (negative) correlations existed between global-averaged precipitation and net longwave fluxes at TOA anomalies at multi-year time-scales. However, for all datasets, the magnitude of $\rho_{P,R_{LW,TOA}}$ at multi-year time-scales was nearly 0.2 lower than for $\rho_{P,R_{LW,SFC}}$. Consequently, a further approximation was considered on the linear model for precipitation fluctuations at multi-year time-scales: $L_V \Delta P \approx c_1 \times (-\Delta R_{atm}) + c_2 \approx c_3 \times (-\Delta R_{LW,net}) + c_4 \approx c_5 \times (-\Delta R_{LW,SFC}) + c_6$. Finally, the surface net longwave radiative flux can be further decomposed into its upwelling and downwelling (henceforth denoted downwelling longwave radiation, DLR) components. Fig. 2d shows that, at multi-year time-scales, the differences in the correlations of global-averaged precipitation against DLR ($\rho_{P,DLR}$) or against net atmospheric radiative fluxes (i.e. $\rho_{P,R_{atm}}$) were within 0.1 in observations, ERA-20C and ERA-20CM (R_{atm} is unavailable for 20CR). Thus, at multi-year time-scales, the fluctuations in downwelling surface longwave radiative fluxes are, to a good approximation, linearly related to precipitation fluctuations: $L_V \Delta P \approx c_7 \times (-\Delta DLR) + c_8$. Notice that the correlation structure of global-averaged precipitation against upwelling surface radiative fluxes or against net atmospheric radiative fluxes are nearly identical in observations. However, significant difference emerged between these two quantities (~0.2) in ERA-20CM and ERA-20C. Thus, a similar linear relationship between ΔP and $\Delta R_{LW,SFC,UP}$ might also hold to a good approximation, although the results are less robust than for ΔP against ΔDLR.

The correlation between global-averaged precipitation and clear-sky net radiative atmospheric heating (i.e. $\rho_{P,R_{atm,cs}}$) was nearly identical to $\rho_{P,R_{atm}}$ at multi-year time-scales (Fig. 3a). This suggested that the cloud effects on the multi-year linear dependence between precipitation variability and net atmospheric radiative fluxes may be neglected. But the same isn't true at time-scales below a few months, where significant differences emerge between $\rho_{P,R_{atm,cs}}$ and $\rho_{P,R_{atm}}$. The clear-sky approximation holds at multi-year time-scales for correlations of global-averaged precipitation against net atmospheric longwave radiative fluxes and, also, and against the global-averaged net surface longwave fluxes (Fig. 3b). Based on these results, it was further hypothesized that cloud effects are also negligible for the correlation between global-averaged precipitation and DLR at multi-year temporal scales. This hypothesis could not be tested directly because clear-sky DLR time-series were not available for the ECMWF datasets. Nonetheless, the results in Section 4 based on an empirical algorithm for DLR estimation under a clear-sky approximation provided support for this hypothesis.

At this point, it is important to notice that the existence of strong correlations does not necessarily imply causality between two variables. However, the atmospheric energy balance in Equation (2) provides a physical basis for the obtained strong (negative) correlations values between precipitation and atmospheric radiative fluxes. In fact, the multi-scale analysis presented here provided further robustness to previous investigations on the importance of energetic constraints to global precipitation, the dominant role of surface longwave fluxes, namely DLR, and the negligible cloud effects in these relationships (e.g., Stephens and Hu, 2010; Stephens et al., 2012a,b). More importantly, a clear transition emerged between robust correlations at multi-year time-scales and negligible correlations at sub-yearly time-scales, which was found for global-averaged precipitation against atmospheric radiative fluxes (particularly total net, net longwave and DLR), global-averaged precipitable water vapor against surface temperature (and SST), for global SST against global near-surface air temperature and, less robustly, for global-averaged precipitation against surface temperature (or SST).

Notice that the correlation structure derived from Haar fluctuations of different combinations of variables presented in the present section are identical to the correlation structure obtained by employing Detrended Cross-Correlation Analysis (DCCA, see Supplementary Figures 1, 2 and 3). DCCA has been previously shown to robustly quantify the correlations at different time-scales (Podobnik & Stanley, 2008; Piao and Fu, 2016; Nogueira, 2017b; 2018, where detailed descriptions of DCCA methodology are also provided). This result provides one of the first empirical verifications for the multi-scale correlation obtained from Haar fluctuations, recently introduced by Lovejoy et al. (2017).

4. Evaluation of the multi-year linear relationships between global-averaged precipitation and clear-sky DLR and surface temperature

The strong correlations between global-averaged precipitation and atmospheric longwave radiative fluxes imply that simple linear model should be able to reproduce the variability precipitation anomalies at multi-year time-scales. This hypothesis is tested in the present section, aiming to provide robustness to the strong multi-year correlations presented in Section 3. Specifically, the robustness of the tight correlation between global-averaged precipitation and clear-sky DLR at multi-year time-scales is tested. Additionally, it is tested whether the more robust correlation between global-averaged precipitation and clear-sky DLR at multi-year time-scales compared to global-averaged precipitation against surface temperature results in a better reconstruction of precipitation variability by such a linear model.

The clear-sky DLR can be derived, to a good approximation, from the global averaged near-surface temperature alone (e.g. Stephens et al., 2012b). Furthermore, given the tight coupling between global-averaged temperature over land and SST at multi-year time-scales (Fig. 1b), it is hypothesized that clear-sky DLR variability could be obtained, to a good approximation directly from the SST forcing. This hypothesis is also supported by the nearly identical correlations between global-averaged precipitable water vapor against surface temperature or against SST (Fig. 1a).

Here two different algorithms to estimate clear-sky DLR are tested: the Dilley-O'Brien model (Dilley & O'Brien, 1998), and the Prata model (Prata, 1996). In the Dilley-O'Brien model:

$$DLR_{2y,DO} = a_1 + a_2 \left(\frac{SST_{2y}}{SST_c}\right)^6 + a_3 \left(\frac{\Delta PWV_{2y}+PWV_c}{PWV_c}\right)^{1/2}, \quad (8)$$

Where $a_1 = 59.38$ Wm^{-2}, $a_2 = 113.7$ Wm^{-2} and $a_3 = 96.96$ Wm^{-2} are the model parameters, and $PWV_c = 22.5$ kg m^{-2} is the climatological value for precipitable water vapor. The subscript '2y' (e.g. DLR_{2y}) indicates a fluctuation for Δt =2-year. Notice that $DLR_{c,DO} = a_1 + a_2 + a_3$ is obtained by replacing the climatological values of PWV and SST in Equation (8).

The Prata model for $\Delta DLR_{2y,Pr}$ is based on the Stefan-Boltzmann equation:

$$DLR_{2y,Pr} = \varepsilon_{clr} \sigma_{SB} {SST_{2y}}^4 \quad (9)$$

Where $\sigma_{SB} = 5.67 \times 10^{-8}$ Wm^{-2}K^{-4} is the Stefan-Boltzmann constant and:

$$\varepsilon_{clr} = 1 - (1 + PWV_{2y})\exp(-(1.2 + 3PWV_{2y})^{1/2}) \quad (10)$$

The anomaly-time series is computed from $\Delta DLR_{2y,Pr} = DLR_{2y,Pr} - DLR_{c,Pr}$, where $DLR_{c,Pr}$ is obtained by replacing the climatological values of PWV and SST in Equations (9) and (10).

The strong correlation between global-averaged precipitable water vapor and SST at multi-year time-scales (Fig. 1a) allowed to remove the PWV dependence in Equations (8) and (11), by replacing $PWV_{2y} \approx \alpha_{PWV,SST} \Delta SST_{2y} + PWV_c$. The forcing ΔSST_{2y} time-series were obtained by coarse-graining the deseasonalized (using Equation (3)) global-averaged SST obtained from GISSTEMP dataset. The sensitivity coefficient, $\alpha_{W,SST} \approx 0.08\ K^{-1}$ was estimated by least-square regression of $\Delta PWV_{2y}/PWV_c$ against ΔSST_{2y}, pooling together all datasets (ERA-20C, ERA-20CM and 20CR). The $\alpha_{PWV,SST}$ estimates are summarized in Table 1, including for each individual dataset, ranging between 0.07 and 0.10 K^{-1}. Notice that the obtained values are close to the typical 0.07 K^{-1} value predicted by the Clausius-Clapeyron relationship.

In this way, two reconstructed anomaly time-series for global-averaged precipitation were obtained using the Diley-O'Brien and the Prata algorithms. The climatological global-averaged precipitation $P_c \approx 2.7$ mm/day was estimated from GPCP dataset. The sensitivity coefficient $\alpha_{P,DLR} \approx 0.004$ (W/m^2)$^{-1}$ was estimated by least-square regression of $\Delta P_{2y}/P_c$ against ΔDLR_{2y}, pooling together all available datasets (ERA-20C, ERA-20CM, 20CR and GPCP against CERES-EBAF). Notice that, in estimating $\alpha_{P,DLR}$, clear-sky DLR time-series were used where available (i.e. for ERA-20C and ERA-20CM) datasets, but they were replaced by (full-sky) DLR otherwise (i.e. for 20CR and CERES-EBAF). The $\alpha_{P,DLR}$ estimates are summarized in Table 2, including values obtained from each dataset (no estimate was made for GPCP against CERES-EBAF due to the limited duration of the latter), ranging between 0.003 $(W/m^2)^{-1}$ and 0.005 $(W/m^2)^{-1}$.

Another simple linear model for reconstruction of multi-year global-averaged precipitation anomaly time-series was tested, based on the direct response (correlations) of P to SST fluctuations, i.e. $P_{2y,SST} \approx \alpha_{P,SST} \Delta SST_{2y} P_c + P_c$. Again, the ΔSST_{2y} was obtained from GISSTEMP dataset. The sensitivity coefficient, $\alpha_{P,SST} \approx 0.02\ K^{-1}$ was estimated by least-square regression of $\Delta P_{2y}/P_c$ against ΔSST_{2y}, pooling together all datasets (ERA-20C, ERA-20CM, 20CR and GPCP against GISSTEMP). The $\alpha_{P,SST}$ estimates are summarized in Table 3, including for each individual dataset, ranging between 0.02 and 0.04 K^{-1}. Notice that the obtained values are close to the 0.01 to 0.03 K^{-1} range reported in the relevant literature (e.g. Schneider et al., 2010; Trenberth, 2011; O'Gorman et al., 2012; and Allan et al., 2014).

When compared against ΔP_{2y} directly derived from GPCP for the 1979 to 2010 period, the errors in the proposed linear ΔP_{2y} reconstructions were generally close to those for atmospheric model-based products (Fig. 4). $\Delta P_{2y,Pr}$ displays the highest mean bias, somewhat higher than for atmospheric model-based datasets, but also higher than the mean bias for $\Delta P_{2y,DO}$ and $\Delta P_{2y,SST}$ (Fig. 4a). Notice that all atmospheric model-based products considered here also display a positive bias. While this may be due a negative bias of GPCP (e.g. Gehne et al., 2015), this observational dataset represents the longest reliable dataset for global precipitation studies and thus was considered here as 'the truth'. More importantly, the mean bias is easy to correct, simply by subtracting its value from the time-series. This correction was implemented here for all atmospheric model-based and linear-model based ΔP_{2y} time-series. Figure 4c shows that the normalized standard deviation ($\sigma_n = \sigma_{2y,model}/\sigma_{2y,obs}$) estimated from $\Delta P_{2y,DO}$ (~0.4) and, particularly, from $\Delta P_{2y,SST}$ (~0.3) were lower than the values estimated from atmospheric model-based products (~0.5-0.9). In contrast, σ_n estimated from $\Delta P_{2y,Pr}$ was nearly 0.8, which was higher than 20CR and most members in the ERA-20CM ensemble, only outperformed by ERA-20C dataset. The root-mean squared error after bias-correction ($RMSE_{bc}$) estimated from $\Delta P_{2y,Pr}$ and $\Delta P_{2y,DO}$ were well within the range of the values obtained from atmospheric model-based products (Fig. 4b), with the Prata model slightly overperforming the Dilley-O'Brien model. $RMSE_{bc}$ estimated from $\Delta P_{2y,SST}$ was on the high-end of the atmospheric model-based range of values, and somewhat worse than for the DLR-based linear models. Finally, the Pearson correlation coefficient between models and observations (Fig. 4d) was similar amongst all linear-based models and well within the range of values estimated from the atmospheric model-based products. The latter result was expected since all linear models were forced by the same SST time-series. Overall, these results suggested that $\Delta P_{2y,Pr}$ (after bias correction) reproduced the observations with similar accuracy to atmospheric model-based products, including similar $RMSE_{bc}$, variability amplitude and phase of the signal. $\Delta P_{2y,DO}$ displayed similar performance for $RMSE_{bc}$ and for the phase, but not for the variability amplitude. Finally, $\Delta P_{2y,SST}$ had the worst performance concerning $RMSE_{bc}$, but also in capturing the variability amplitude, while it displayed similar ability to the other linear models in reproducing the phase. The overall weakest performance of $\Delta P_{2y,SST}$ was coherent with the less robust correlations underlying this model. Additionally, the results indicate that the non-linear transformations on SST employed in the Prata and the Dilley-O'Brien algorithms improved the linear models.

5. Exploring scale-invariance for stochastic downscaling of precipitation to monthly resolution

At sub-yearly time-scales, the magnitude of the correlations between global-averaged precipitable water vapor and SST, precipitation and DLR, and precipitation and SST decreases abruptly to negligible values (cf. Section 3). Additionally, the cloud-effects on the energetic constraints of precipitation variability become non-negligible (Fig. 3). Consequently, the linear relationships underlying the above simple linear reconstructions of global-averaged precipitation at 2-year resolution are no longer appropriate at sub-yearly time-scales. Previous investigations have suggested that this transition should be related to a fundamental transition in the stochastic scale-invariant behavior of climate variables, which separates a high-frequency weather regime that extends up to about the synoptic scales (around 10 days to 1-month in the atmosphere, and around 1-year in the oceans) from a low-frequency weather (or macroweather) regime that extends up to a few decades (see e.g. Lovejoy et al., 2017; Nogueira, 2018). In the weather regime the amplitude of the fluctuations tends to increase with time-scale, while in the macroweather regime the amplitude of the fluctuations tends to decrease with increasing time-scale, hence implying a convergence toward the 'climate normal' at time-scales of a few decades (Lovejoy, 2015).

In the present section, it is shown that the multi-scale analysis framework can also be taken advantage to perform stochastic downscaling from the multi-year to monthly resolution. This exercise allows to demonstrate the relevance of understanding and characterizing the multi-scale structure of atmospheric variables and its remarkable potential for stochastic downscaling applications.

Building on the strong scale-invariant symmetries present in the variability of global and regional precipitation across wide ranges of time-scales (e.g. Lovejoy and Schertzer, 2013; Nogueira et al., 2013; Nogueira and Barros, 2014, 2015; Nogueira, 2017, 2018), an algorithm was proposed here to derive the sub-yearly statistics from the multi-year information alone. The physical basis for this algorithm is that while the atmosphere is governed by continuum mechanics and thermodynamics, it simultaneously obeys statistical turbulence cascade laws (e.g., Lovejoy & Schertzer, 2013; Lovejoy et al., 2018).

Conveniently, precipitation (and many other atmospheric variables) is characterized by low spectral slopes $\beta < 1$, with quasi-Gaussian and quasi-non-intermittent statistics, at time-scales between ~10 days and a few decades (Lovejoy & Schertzer, 2013; de Lima & Lovejoy, 2015; Lovejoy et al., 2015, 2017; Nogueira, 2017b, 2018). Grounded by these scale-invariant properties, fractional Gaussian noise was used here to generate multiple realizations of downscaled ΔP at monthly resolution from each member of each ΔP_{2y} time-series:

$$\Delta P_{1m}(t) = fGn_{1m}(t)\,\frac{\Delta P_{2y}(t)}{fGn_{2y}(t)} \tag{11}$$

where fGn_{1m} is a fractional Gaussian noise, which was computed by first generating a random Gaussian noise (g), then taking its Fourier transform $(\tilde{g})$, multiplying by $k^{-\beta/2}$, and finally taking the inverse transform to obtain fGn_{1m}. The mean of fGn_{1m} was forced to be equal to the number of data-points of ΔP_{2y}. Then fGn_{2y} was obtained by coarse-graining fGn_{1m}using 24-point (i.e. 2 years) length boxes. In this way, $\Delta P_{1m,DO}$, $\Delta P_{1m,Pr}$, $\Delta P_{1m,SST}$ ensembles are generated respectively from the bias-corrected $\Delta P_{2y,DO}$, $\Delta P_{2y,Pr}$ and $\Delta P_{2y,SST}$ time-series. One hundred plausible realizations are generated for each ensemble, corresponding to one hundred different realizations of fGn_{1m}. Based on recent investigations on P scale-invariance properties, a spectral exponent $\beta \approx 0.3$ is assumed (de Lima & Lovejoy, 2015; Nogueira, 2018). In Equation (11), the 2-year resolution time-series were assumed to have a constant value for every month inside each 2-years period.

Notice that a resolution limit should exist to the proposed stochastic downscaling algorithm, namely at time-scales below ~10 days where a fundamental transition occurs in the scaling behavior of most atmospheric fields (including global-averaged precipitation, see e.g. Lovejoy & Schertzer, 2013; Lovejoy, 2015; de Lima & Lovejoy, 2015; Nogueira, 2017a,b, 2018). At faster time-scales intermittency becomes non-negligible and the quasi-Gaussian approximation to the statistics is no longer robust.

The proposed downscaling methodology corresponds to treating the sub-yearly frequencies as random 'weather noise', which is characterized, to a good approximation, by scale-invariant behavior with quasi-Gaussian statistics (Vallis, 2009; Lovejoy et al., 2015). A similar downscaling methodology has been previously demonstrated to reproduce the spatial sub-grid scale variability of topographic height (Bindlish & Barros, 1996), precipitation (Bindlish & Barros, 2000; Rebora et al., 2006; Nogueira et al., 2013; Nogueira & Barros, 2015) and clouds (Nogueira & Barros, 2014).

Figure 5a showed that the PDFs computed from $\Delta P_{1m,DO}$, $\Delta P_{1m,Pr}$ and $\Delta P_{1m,SST}$ were in remarkable agreement with PDFs obtained from GPCP observational dataset for the 1979-2010 period, representing a significant improvement compared to all atmospheric model-based products. This improved PDF accuracy was quantified using the Perkins skill score, S-Score (Perkins et al., 2007), defined as:

$$\text{S-Score}=100 \times \sum_{i=1}^{M} min[f_{mod}(i), f_{obs}(i)] \quad (12)$$

where $f_{mod}(i)$ and $f_{obs}(i)$ are respectively the frequency of the modeled and observed P anomaly values in bin i, M is the number of bins used to compute the PDF (here M=15), and min[x,y] is the minimum between the two values. The S-Score is a measure of similarity between modeled and observed PDFs, such that if a model reproduces the observed PDF perfectly then S-Score=100%.

The linear-based models showed S-Score values around 95%, which were significantly higher than then ~80% found for the atmospheric model-based products (Fig. 6). Furthermore, the stochastic model captured the change in the PDFs between two separate periods (1979-1990 and 1999-2010, Fig. 5b), while preserving the remarkably high (≥90%) S-Scores (Fig. 6, blue and red markers). Indeed, the S-Scores for linear-based were consistently better than the S-Scores obtained from atmospheric model-based products (~80%). Despite some differences between PDFs obtained from $\Delta P_{1m,DO}$, $\Delta P_{1m,Pr}$ and $\Delta P_{1m,SST}$, their similar performance in reproducing observations was somewhat unexpected, given the distinct performances in reproducing the observed time-series at multi-year resolutions. While the error analysis here was based on a limited sample (mainly due to short duration of the satellite-period), these results suggested that the proposed stochastic downscaling mechanism is quite robust in reproducing the monthly statistics of global-averaged precipitation, with only moderate sensitivity to the coarse resolution forcing.

6. Discussion and Conclusions

Atmospheric variables display significant variability over a wide range of temporal scales, both due changes in external forcings (including surface fluxes, changes to greenhouse gases and aerosol concentrations, solar forcing, and volcanic eruptions), but also due to intrinsic modes of atmospheric variability. Additionally, external and internal atmospheric processes interact nonlinearly amongst themselves, resulting in an intricate multi-scale structure, which is still ill understood and responsible for significant uncertainties in climate models. Here a multi-scale analysis framework was employed, aiming to disentangle the complex structure of global-averaged precipitation variability. The multi-scale correlation structure obtained from Haar fluctuations suggested that global-mean precipitation variability at multi-year time-scales is linearly related to the net atmospheric radiative fluxes, corresponding to the dominant effect of energetic constraints on precipitation variability. Furthermore, this linear relationship is dominated by its longwave component and, more specifically, by the surface longwave radiative fluxes, particularly DLR. The results also suggest that clouds play a negligible effect in these linear correlations at multi-years scales.

Building on previous works of Lovejoy et al. (2017) and Nogueira (2018), the present manuscript highlights a critical transition in the multi-scale correlation structure at time-scales ~1-year, revealing a change in the control mechanisms of several atmospheric variables, including precipitation. Specifically, at multi-year time-scales: (i) global-averaged precipitation becomes tightly correlated to the net atmospheric radiative fluxes ($|\rho| \gtrsim 0.8$), and this correlation is dominated by the downwelling longwave radiative flux at the surface; (ii) the cloud effects on the atmospheric radiative fluxes in (i) can be neglected; (iii) global-averaged precipitable water vapor becomes tightly correlated (ρ~0.9) to surface temperature. The respective sensitivity coefficient for multi-year fluctuations of precipitable water vapor to surface temperature is estimated here to be 0.07%/K, close to the value predicted by the Clausius-Clapeyron relationship; (iv) global-averaged SST and near-surface air temperature over land become strongly correlated

($\rho \sim 0.7$), implying a strong atmosphere-ocean coupling in agreement and extending the results from Lovejoy et al. (2017) based on one observational dataset. In contrast, at sub-yearly time-scales, the magnitude of all these correlations decreases abruptly towards negligible values, and cloud effects are no longer negligible in the correlations between atmospheric radiative fluxes and precipitation. Hints of a similar, but less robust, transition also emerged for the correlation structure between global-averaged precipitation and surface temperature - with negligible correlations at sub-yearly time-scales, which tend increase at multi-year time-scales, although the latter displayed significant spread amongst different datasets (ranging between ~0.4 to ~0.7).

The transition found here also contributes to sharpen the picture from previous studies reporting a 'slow' response where global-averaged precipitation increases due to increasing surface temperature, and a 'fast' response in which the atmosphere rapidly adjusts to changes in top of atmosphere radiative forcing, and that is independent of temperature fluctuations (Allen & Ingram, 2002; Bala et al., 2010; Andrews et al., 2010; O'Gorman et al., 2012; Allan et al., 2014). The correlation structure found here suggests that the 'slow' component corresponds to multi-year time-scales, and that radiative constraints (particularly surface longwave fluxes) are the key mechanism controlling precipitation variability rather than temperature, while cloud effects are negligible. On the other hand, the correlations here confirm the break down of the linear relation between temperature fluctuations at fast (sub-yearly) time-scales, but the dominant effect of top of atmosphere radiative forcing is not evident and, most likely, the situation is much more complex (for example surface sensible heat fluxes seem to become relevant at these time-scales).

The robustness of this emergent multi-scale correlation structure is demonstrated by proposing simple models for reconstruction of global-averaged at multi-year time-scales. Anomaly time-series for global-averaged precipitation at 2-year resolution were derived from SST observations alone, either directly based on precipitation vs SST correlation structure, or by combining the more robust energetic constraints of global-averaged precipitation (namely the precipitation vs clear-sky DLR correlation) with empirical algorithm for clear-sky DLR estimation, and the Clausius-Clapeyron relationship. After correcting for their systematic mean bias, the highly-idealized model for ΔP_{2y} based on clear-sky DLR estimated from the Prata algorithm displayed similar accuracy in reproducing observations as atmospheric model-based products, as measured by $RMSE_{bc}$, Pearson correlation coefficient and normalized standard deviation. Finally, the model based on precipitation vs SST correlation showed the weakest performance, which agrees with the less robust correlations underlying this idealized model.

The proposed linear models cannot be extended to sub-yearly the time-scales because all the correlations upon which they rely become negligible. This abrupt transition in the multi-scale correlation structure implies that at sub-yearly time-scales the tight linear coupling between atmospheric and ocean temperature, the Clausius-Clapeyron relationship, and the atmospheric energy balance are no longer dominant linear constraints for global-averaged. Nonetheless, the multi-scale analysis framework provides another path for reconstruction of the precipitation statistics at sub-yearly resolution. A stochastic downscaling algorithm based on scale-invariant symmetries of precipitation was applied to ΔP_{2y} reconstructed time-series, resulting in monthly global-averaged precipitation PDFs. Remarkably, the reconstructed PDFs at monthly resolution showed better accuracy in reproducing observed statistics than atmospheric model-based products, as measured by the PDF matching S-Score computed over decadal and 30-year periods. These results highlight the relevance and potential applications of multi-scale frameworks for atmospheric sciences.

Acknowledgements

The author would like to thank Shaun Lovejoy for his detailed comments and suggestions and for making available the codes for computing the Haar fluctuations. The author also thanks the anonymous reviewer for his comments and suggestions, which helped to improve the manuscript. This study was funded by the Portuguese Science Foundation (F.C.T.) under project CONTROL (PTDC/CTA-MET/28946/2017). The author was funded by the Portuguese Science Foundation (F.C.T.) under grant UID/GEO/50019/2013.

ERA-20C and ERA-20CM were provided by ECMWF and are available through the website http://apps.ecmwf.int/datasets.

20CR reanalysis, GISSTEMP and GPCP precipitation product were provided by the NOAA/OAR/ESRL PD, Boulder, Colorado, USA, from their website http://www.esrl.noaa.gov/psd.

The CERES-EBAF data were obtained from the NASA Langley Research Center Atmospheric Science Data Center, from their website https://eosweb.larc.nasa.gov/project/ceres/ebaf_surface_table

References

Adler, R. F., Huffman, G. J., Chang, A., Ferraro, R., Xie, P.-P., Janowiak, J., Rudolf, B., Schneider, U., Curtis, S., Bolvin, D., Gruber, A., Susskind, J., Arkin, P., and Nelkin, E.: The Version-2 Global Precipitation Climatology Project (GPCP) monthly precipitation analysis (1979–Present), J. Hydrometeorol., 4(6), 1147–1167, doi:10.1175/1525-7541(2003)004<1147:TVGPCP>2.0.CO;2, 2003.

Allan, R. P., Liu, C., Zhan, M., Lavers, D. A., Koukouvagias, E., and Bodas-Salcedo, A.: Physically consistent responses of the global atmospheric hydrological cycle in models and observations. Surv. Geophys. **35**, 533-552, 2014.

Allen, M.R., and Ingram, W. J.: Constraints on future changes in climate and the hydrologic cycle. Nature **419**, 224-232, 2002.

Andrews, T., Forster, P. M., Boucher, O., Bellouin, N., and Jones, A.: Precipitation, radiative forcing and global temperature change. Geophys. Res. Lett. **37**, L14701, 2010.

Bala, G., Caldeira, K., and Nemani, R.: Fast versus slow response in climate change: Implications for the global hydrological cycle. Clim. Dyn. **35**, 423-434, 2010.

Bindlish, R., and Barros, A. P.: Aggregation of digital terrain data using a modified fractal interpolation scheme. Comput. Geosci. (UK) **22**, 907-917, 1996.

Bindlish, R., & Barros, A. P.: Disaggregation of rainfall for one-way coupling of atmospheric and hydrological models in regions of complex terrain. Global Planet. Chang, **25(12)**, 111-132, 2000.

Collins, M., Knutti, R., Arblaster, J., Dufresne, J.-L., Fichefet, T., Friedlingstein, P., Gao, X., Gutowski, W. J., Johns, T., Krinner, G., Shongwe, M., Tebaldi, C., Weaver, A. J., and Wehneret, M.: Long-term climate change: Projections, commitments and irreversibility, in Climate Change 2013: The Physical Science Basis. Contribution of Working Group I to the Fifth Assessment Report of the Intergovernmental Panel on Climate Change, edited by T. F. Stocker et al., pp. 1029–1136, Cambridge Univ. Press, Cambridge, U. K., and New York, 2013.

Compo, G. P., Whitaker, J. S., Sardeshmukh, P. D., Matsui, N., Allan, R. J., Yie, X., Gleason, B. E., Vose, R. S., Rutledge, G., Bessemoulin, P., Brönimann, S., Brunet, M., Crouthamel, R. I., Grant, A. N., Groisman, P. Y., Jones, P. D., Kruk, M. C., Kruger, A. C., Marshall, G. J.,Maugeri, M., Mok, H. Y., Nordli, O., Ross, T. F., Trigo, R. M., Wang, X. L., Woodruff, S. D., and Worley, S. J.: The Twentieth Century Reanalysis Project. Q. J. R. Meteorol. Soc. **137**, 1-28, 2011.

Dilley, A. C., and O'Brien, D.M.: Estimating downward clear-sky long-wave irradiance at the surface from scree temperature and precipitable water. Q. J. R. Meteorol. Soc. **124A**, 1391-1401, 1998.

Gehne, M., Hamill, T. M., Kiladis, G. N., and Trenberth, K. E.: Comparison of Global Precipitation Estimates across a Range of Temporal and Spatial Scales. J. Clim. **29**, 7773-7795, 2016.

Gu G, and Adler R. F.: Precipitation and temperature variations on the interannual time scale: assessing the impact of ENSO and volcanic eruptions. J Clim 24:2258–2270, 2011.

Gu, G. and Adler, R. F.: Large-scale, inter-annual relations among surface temperature, water vapour and precipitation with and without ENSO and volcano forcings. Int. J. Climatol., 32: 1782–1791. doi:10.1002/joc.2393, 2012.

Hansen, J., R. Ruedy, M. Sato, and Lo, K.: Global surface temperature change, Rev. Geophys., 48, RG4004, doi:10.1029/2010RG000345, 2010.

Hegerl, G. C., Black, E., Allan, R. P., Ingram, W. J., Polson, D., Trenberth, K., Chadwick, R. S., Arkin, P. A., Sarojini, B. B., Becker, A., Dai, A., Durack, P. J., Easterling, D., Fowler, H. J., Kendon, E. J., Huffman, G. J., Lu, C., Marsh, R., New, M., Osborn, T. J., Skliris, N., Stott, P. A., Vidale, P.-L., Wijffels, S. E., Wilcox, L. J., Willet, K. M., and Zhang, X.: Challenges in quantifying changes in the global water cycle. Bull. Am. Meteorol. Soc. **96**, 1097–1115, 2015.

Held, I. M. and Soden, B. J.: Robust responses of the hydrological cycle to global warming. J. Clim. **19**, 5686-5699, 2006.

Hersbach, H., Peubey, C., Simmons, A., Berrisford, P., Poli, P. and Dee, D. P.: ERA-20CM: A twentieth century atmospheric model ensemble. Q. J. R. Meteorol. Soc. **141**, 2350-2375, 2015.

de Lima, M. I. P. and Lovejoy, S.: Macroweather precipitation variability up to global and centennial scales. Water. Resour. Res. **51**, 9490-9513, 2015.

Loeb, N. G., Wielicki, B. A., Doeling, D. R., Smith, G. L., Keyes, D. F., Kato, S., Manalo-Smith, N., and Wong, T.: Toward Optimal Closure of the Earth's Top-of-Atmosphere Radiation Budget. J. Clim. **22**, 748-766, 2009.

Lovejoy S, and Schertzer, D.: The Weather and Climate: Emergent Laws and Multifractal Cascades, Cambridge University Press, Cambridge, 2013.

Lovejoy, S.: A voyage through scales, a missing quadrillion and why the climate is not what you expect, Clim. Dynam., 44, 3187–3210, 2015.

Lovejoy, S., del Rio Amador, L. and Hébert, R.: The ScaLIng Macroweather Model (SLIMM): Using scaling to forecast global-scale macroweather from months to decades. Earth System Dynamics **6**, 1-22, 2015.

Lovejoy, S., Del Rio Amador, L., and Hébert, R.: Harnessing butterflies: theory and practice of the Stochastic Seasonal to Interannual Prediction System (StocSIPS), in Tsonis A. (eds) Advances in Nonlinear Geosciencs, Springer, Cham, 2017.

Nogueira, M., Barros, A. P., and Miranda, P. M. A.: Multifractal properties of embedded convective structures in orographic precipitation: toward subgrid-scale predictability. Nonlin. Processes Geophys., 20, 605-620, doi:10.5194/npg-20-605-2013, 2013.

Nogueira, M., and Barros, A. P.: The nonconvective/convective structural transition in stochastic scaling of atmospheric fields. J. Geophys. Res. Atmos. **119**, 771-794, 2014.

Nogueira, M., & Barros, A. P.: Transient stochastic downscaling of quantitative precipitation estimates for hydrological applications. J.Hydrol. **529(3)**, 1407-1421, 2015.

Nogueira, M.: Exploring the link between multiscale entropy and fractal scaling behavior in near-surface wind. PLoS ONE 12(3): e0173994. https://doi.org/10.1371/journal.pone.0173994, 2017a.

Nogueira, M.: Exploring the links in monthly to decadal variability of the atmospheric water balance over the wettest regions in ERA-20C. J. Geophys. Res.: Atmos. **122**,560–577, 2017b.

Nogueira, M.: The sensitivity of the atmospheric branch of the global water cycle to temperature fluctuations at synoptic to decadal time-scales in different satellite- and model-based products. Clim. Dyn. https://doi.org/10.1007/s00382-018-4153-z, 2018.

O'Gorman, P. A., Allan, R. P., Byrne, M. P. and Previdi, M.: Energetic constraints on precipitation under climate change. Surv. Geophys. **33**, 585-608, 2012.

Pauluis, O., & Held, I.: Entropy budget of an atmosphere in radiative-convective equilibrium. Part I: Maximum work and frictional dissipation, J. Atmos. Sci., 59, 125-139, https://doi.org/10.1175/1520-0469(2002)059<0125:EBOAAI>2.0.CO;2, 2002.

Perkins, S., Pitman, A., Holbrook, N. and McAneney, J.: Evaluation of the AR4 Climate Models' Simulated Daily Maximum Temperature, Minimum Temperature, and Precipitation over Australia Using Probability Density Functions. J. Clim. **20**, 4356-4376, 2007.

Podobnik, B., and Stanley, H. E.: Detrended Cross-Correlation Analysis: A New Method for Analyzing Two Nonstationary Time-Series. Phys. Rev. Lett. **100**, 084102, 2008.

Podobnik, B., Jiang, Z., Zhou, W. & Stanley, H. E.: Statistical tests for power-law cross-correlated processes. Phys. Rev. E **84**, 06618, 2011.

Poli, P., Hersbach, H., Dee, D. P., Berrisford, P., Simmons, A. J., Vitart, F., Laloyaux, P., Tan, D., Peubey, C., Thépaut, N., Trémolet, Y., Hólm, E. V., Bonavita, M., Isaksen, L., and Fisher, M.: ERA-20C: An Atmospheric Reanalysis for the Twentieth Century. J. Clim. **29**, 4083-4097, 2015.

Prata, A. J.: A new long-wave formula for estimating downward clear-sky radiation at the surface. Q. J. R. Meteor. Soc. **122**, 1127-1151, 1996.

Rebora, N., Ferraris, L., von Hardenberger, J., and Provenzale, A.: RainFARM: Rainfall downscaling by a filtered autoregressive model, J. Hydrometerol., 7, 724-738, 2006.

Schneider, T., O'Gorman, P. A. and Levine, X. J.: Water vapor and the dynamics of climate changes. Rev. Geophys. **48**, RG3001, 2010.

Stephens, G. L. and Ellis, T. D.: Controls of global-mean precipitation increases in global warming GCM experiments. J. Clim. **21**, 6141-6155, 2008.

Stephens, G. L., and Hu, Y.: Are climate-related changes to the character of global precipitation predictable? Environ. Res. Lett. **5**, 025209, 2010.

Stephens, G. L., Li, J., Wild, M., Clayson, C. A., Loeb, N., Kato, S., L'Ecuyer, T., Stackhouse Jr., P. W., Lebsock, M., and Andrews, T.: An update on Earth's energy balance in light of the latest global observations. Nat. Geosci. **5**, 691-696, 2012a.

Stephens, G. L., Wild, M., Stackhouse Jr., P. W., L'Ecuyer, T., Kato, S., and Henderson, D. S.: The global character of the flux of downward longwave radiation. J. Clim. **25**, 557-571, 2012b.

Trenberth, K. E.: Changes in precipitation with climate change, Clim. Res., 47, 123–138, 2011.

Vallis, G. K.: Mechanisms of climate variability from years to decades. In Palmer, T. N.., & Williams, P. (eds.) Stochastic Physics and Climate Modelling, 1-34, Cambridge University Press, Cambridge, 2009.

Xie, P., and Arkin, P. A.: Global Monthly Precipitation Estimates from Satellite-Observed Outgoing Longwave Radiation, J. Climate, 11, 137-164. https://doi.org/10.1175/1520-0442(1998)011<0137:GMPEFS<2.0.CO;2, 1998.

Table 1 Linear regression coefficient $\alpha_{W,SST}$ estimated from ΔPWV/PWV_c against ΔSST at 2-year resolution, assuming a relationship as given by Equation (1). The respective coefficient of determination is also provided. The $\alpha_{W,SST}$ are computed for ERA-20C, 20CR, and for the ensemble of ERA-20CM simulations. Additionally, the coefficient is estimated by pooling together ERA-20C, ERA-20CM (ensemble) and 20CR datasets.

Dataset	$\alpha_{PWV,SST}$ $[K^{-1}]$	R^2
ERA-20C	0.09	0.97
20CR	0.10	0.92
E20CM (Ensemble)	0.07	0.92
All Datasets	0.08	0.91

Table 2. Linear regression coefficient $\alpha_{P,DLR}$ estimated from ΔP/P_c against ΔDLR at 2-year resolution, assuming a relationship as given by Equation (11). The respective coefficients of determination are also provided. The $\alpha_{P,DLR}$ values are computed for ERA-20C, 20CR, and for the ensemble of ERA-20CM simulations. Additionally, the coefficient is estimated by pooling together all datasets, including GPCP observations against DLR from CERES-EBAF.

Dataset	$\alpha_{P,DLR}$ $[(Wm^{-2})^{-1}]$	R^2
ERA-20C	0.005	0.88
20CR	0.003	0.51
E20CM (Ensemble)	0.004	0.81
All datasets (includes observations)	0.004	0.70

Table 3. Linear regression coefficient $\alpha_{P,SST}$ estimated from ΔP/P_c against ΔSST at 2-year resolution. The respective coefficients of determination are also provided. The $\alpha_{P,SST}$ values are computed for ERA-20C, 20CR, for the ensemble of ERA-20CM simulations, and for GPCP against ERA-20CM control SST forcing. Additionally, the coefficient is estimated by pooling together all datasets.

Dataset	$\alpha_{P,SST}$ $[K^{-1}]$	R^2
ERA-20C	0.04	0.89
20CR	0.02	0.35
E20CM (Ensemble)	0.02	0.73
GPCP	0.04	0.42
All datasets (includes observations)	0.02	0.53

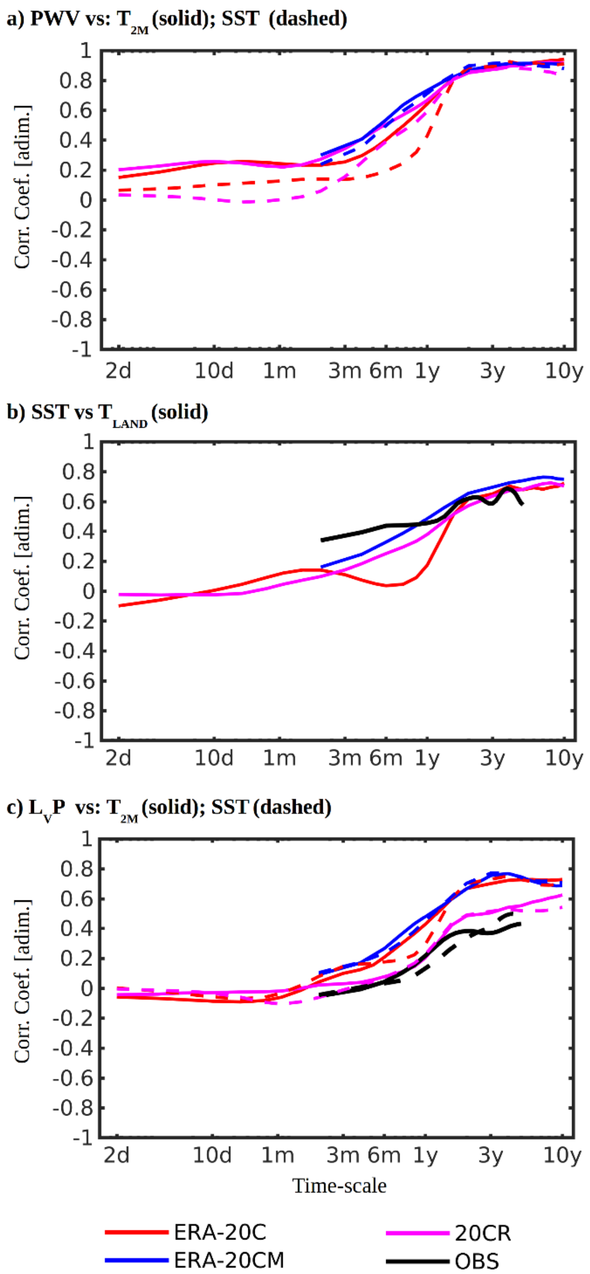

Figure 1. Cross-correlation coefficients against temporal scale computed from Haar fluctuations for global-mean time-series of a) PWV vs T_{2m} (solid) and PWV vs SST (dashed); b) SST vs T_{land}; and c) L_vP vs T_{2m} (solid) and L_vP vs SST (dashed). Red lines represent results from ERA-20C, blue lines from ERA-20CM, pink lines are from 20CR and black lines are estimated from observational products.

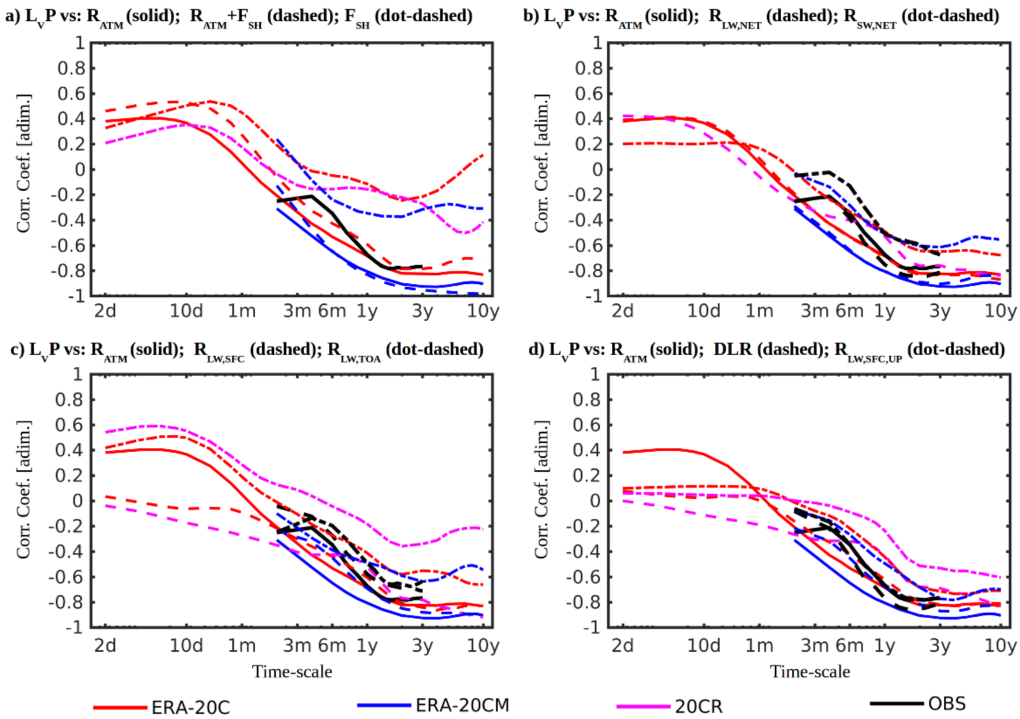

Figure 2. Cross-correlation coefficients against temporal scale computed from Haar fluctuations of a) L_vP vs R_{atm} (solid), L_vP vs $(R_{atm} + F_{SH})$ (dashed) and L_vP vs F_{SH} (dot-dashed); b) L_vP vs R_{atm} (solid), L_vP vs $R_{LW,net}$ (dashed), and L_vP vs $R_{SW,net}$ (dot-dashed); c) L_vP vs R_{atm} (solid), L_vP vs $R_{LW,SFC}$ (dashed), and L_vP vs $R_{LW,TOA}$ (dot-dashed); and d) L_vP vs R_{atm} (solid), L_vP vs DLR (dashed), and L_vP vs $R_{LW,SFC,UP}$ (dot-dashed). Red lines are computed from ERA-20C, blue lines are from ERA-20CM, pink lines are from 20CR and black lines are computed from GPCP and CERES-EBAF observational products. Notice that R_{atm} and $R_{SW,net}$ weren't available from 20CR, while sensible heat flux wasn't available from observations.

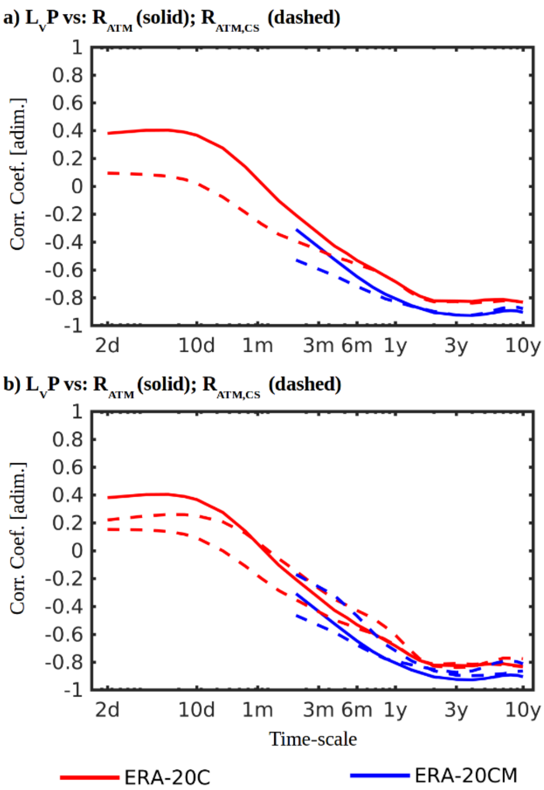

Figure 3. Cross-correlation coefficients against temporal scale computed from Haar fluctuations of a) $L_v P$ vs R_{atm} (solid) and $L_v P$ vs $R_{atm,CS}$ (dashed); b) $L_v P$ vs $R_{LW,SFC}$ (solid) and $L_v P$ vs $R_{LW,SFC,CS}$ (dashed). Red lines are computed from ERA-20C and blue lines are from ERA-20CM.

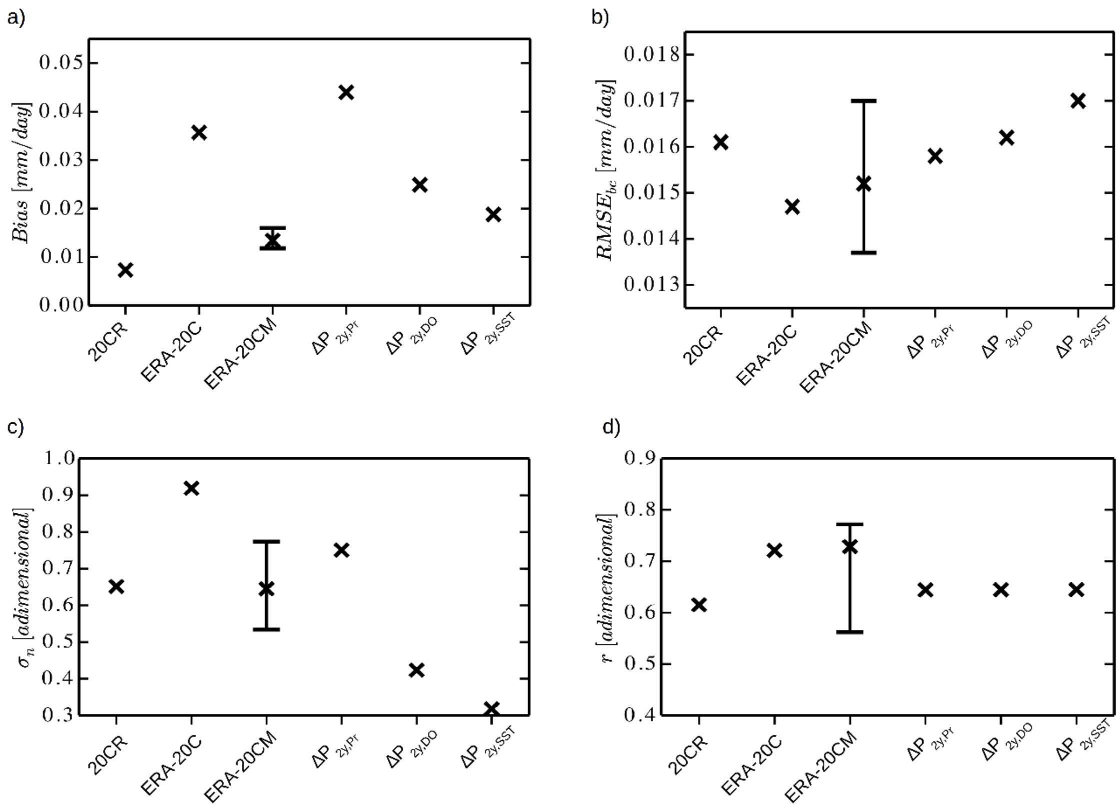

Figure 4. Error estimates from simulated anomaly time-series for P at 2-year resolution against GPCP, computed for the 1979-2010 period, including a) mean bias (Bias); b) root-mean-square error after bias correction ($RMSE_{bc}$); c) model standard deviation normalized by observed standard deviation (σ_n); and d) Pearson correlation coefficient (r). For ERA-20CM dataset the range for all ensemble members is shown, while 'x' marks their mean value. The p-value for all correlations shown in panel (d) are <0.05.

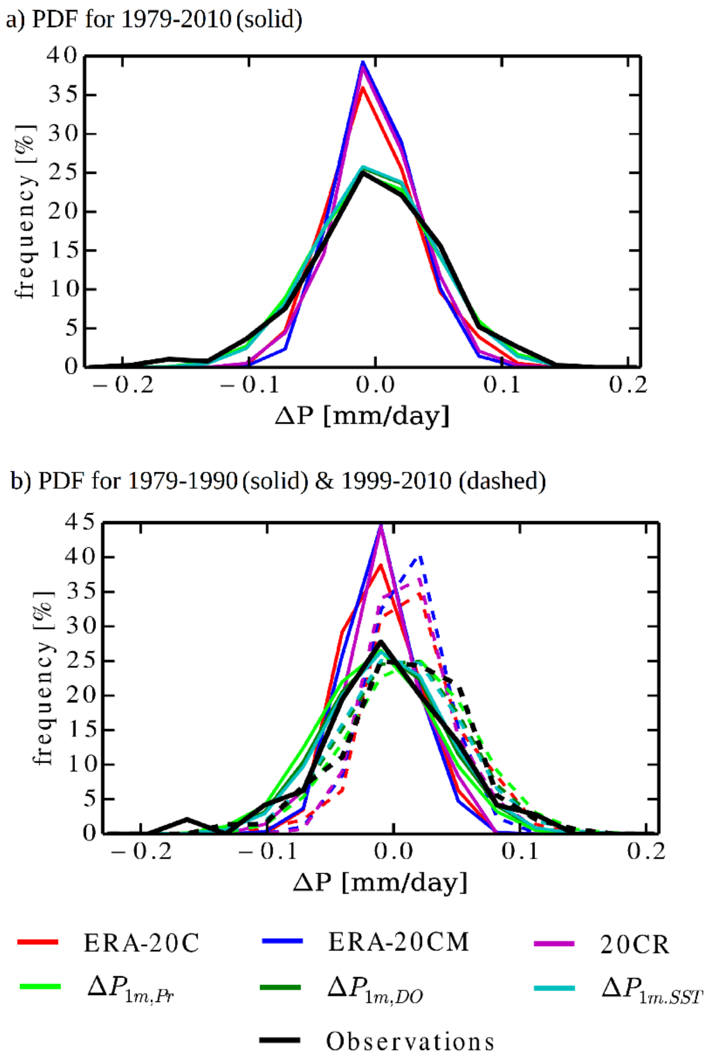

Figure 5. PDFs estimated from monthly anomaly time-series for P from ERA-20C (red), ERA-20CM (dark blue), 20CR (pink), GPCP (black), $\Delta P_{1m,DO}$ (dark green), $\Delta P_{1m,Pr}$ (light green), and $\Delta P_{1m,SST}$ (light blue). In panel a) the PDFs are estimated for the 1979-2010 period, and in panel b) the PDFs are estimated for the 1979-1990 period (solid) and the 1999-2010 period (dashed).

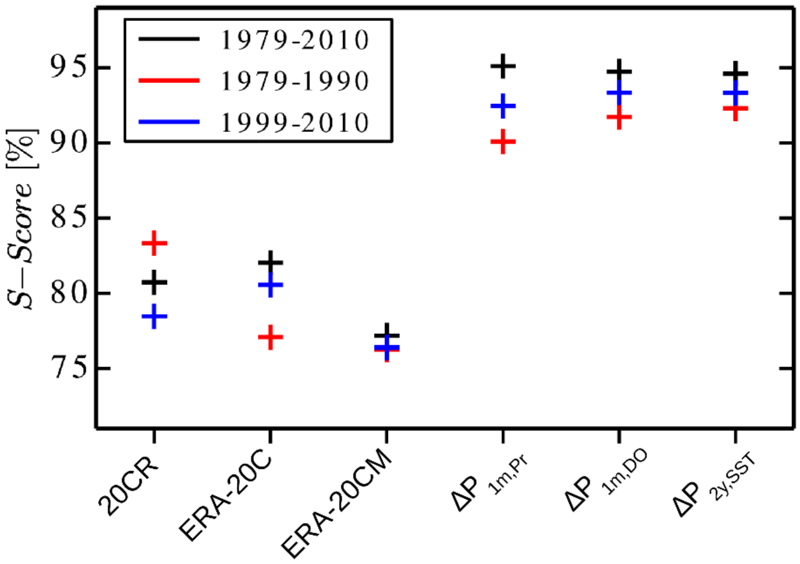

Figure 6. S-Score computed from the different P simulations against GPCP. The values estimated for the full satellite period (1979-2010) are presented in black, for the 1979-1990 period are presented in red, and for 1990-2010 period are presented in blue. For ERA-20CM dataset, the S-Score is estimated from the 10-member ensemble PDF.